

Robust nonequilibrium pathways to microcompartment assembly

Grant M. Rotskoff,^{1,2} Phillip L. Geissler,^{2,3*}

¹Courant Institute of Mathematical Sciences, New York University,
251 Mercer St., New York, NY 10012, USA

²Department of Chemistry, University of California, Berkeley CA 94720, USA

*To whom correspondence should be addressed; E-mail: geissler@berkeley.edu.

Cyanobacteria sequester photosynthetic enzymes into microcompartments which facilitate the conversion of carbon dioxide into sugars. Geometric similarities between these structures and self-assembling viral capsids have inspired models that posit microcompartments as stable equilibrium arrangements of the constituent proteins. Here we describe a different mechanism for microcompartment assembly, one that is fundamentally nonequilibrium and yet highly reliable. This pathway is revealed by simulations of a molecular model resolving the size and shape of a cargo droplet, and the extent and topography of an elastic shell. The resulting metastable microcompartment structures closely resemble those of carboxysomes, with a narrow size distribution and faceted shells. The essence of their assembly dynamics can be understood from a simpler mathematical model that combines elements of classical nucleation theory with continuum elasticity. These results highlight important control variables for achieving nanoscale encapsulation in general, and for modulating the size

and shape of carboxysomes in particular.

Spatial segregation is an ubiquitous strategy in biology for organizing the crowded, active viscera of the cell (1–4). Viral capsids exemplify this organization at very small scales, sequestering genetic material from the cytosol and recapturing it for delivery to new hosts. Extensive work has explored the structure, stability, and assembly dynamics of viruses, highlighting generic design principles and physical origins of the spontaneous assembly process (5–10). Overall capsid structure typically follows from the arrangements of neighboring proteins that are preferred by their noncovalent interactions. Strong preferences yield regular and highly stable structures, but at the same time impair kinetic accessibility by producing deep kinetic traps (11).

Bacterial microcompartments serve a very different biomolecular purpose from viruses but have striking structural similarities, namely, a quasi-icosahedral protein shell that assembles around a fluctuating cargo (2, 12–14). This comparison raises the question: Do the same assembly principles, based on a balance between equilibrium stability and kinetic accessibility, apply to microcompartments as well? Here we focus on a paradigmatic example of a microcompartment, the carboxysome. Carboxysomes play an essential role in the carbon fixation pathway of photosynthetic cyanobacteria (15). The shell proteins of the carboxysome, which have hexameric and pentameric crystallographic structures, assemble to encapsulate a condensed globule of protein including the enzymes RuBisCO and carbonic anhydrase (16–18). These vital, organelle-like structures regulate a microscopic environment to enhance catalytic efficiency, which has made them an attractive target for bioengineering applications (19–22).

Like some viral capsids, carboxysomes feature pronounced facets and vertices, and crystal structures of shell components suggest highly symmetric local protein arrangements (16, 18, 23). Unlike in viral capsids, however, these apparent preferences do not directly indicate the assembled structure, nor do they clearly point to a characteristic microcompartment size (24).

Indeed, experimental evidence has not constrained a particular mechanism for assembly: live cell images support the notion that the cargo assembles first and is subsequently coated by the shell (12), while direct observations of partially formed carboxysomes in electron micrographs point to a cooperative mechanism for assembly (25). Identifying essential variables for controlling or emulating carboxysome assembly awaits a clearer understanding of its dynamical pathways and underlying driving forces.

Theoretical and computational models for nanoshell assembly have primarily followed approaches inspired by viral capsid assembly. These approaches have emphasized the role of preferred curvature and shell-cargo interactions as a template for the final structure (26). In the absence of cargo, it has been shown that successful assembly of empty shells with an intrinsic curvature can occur under an irreversible dynamics (27, 28). Here we introduce and explore a model based on a different mechanistic perspective. The basic components are a cargo species that is prone to aggregation, a shell species that spontaneously forms flat elastic sheets, and an attractive interaction between the inside of the shell and the cargo, depicted in Figs. 1A, S1-S3. Thermodynamic considerations imply that finite encapsulated structures in such a system have negligible weight at equilibrium (Sec. S3). Nevertheless, we show that regularly sized microcompartments can emerge reliably in the course of natural dynamics.

Fig. 1 depicts an example assembly pathway of this molecular model. Trajectories are initiated with a small droplet of cargo and a handful of proximate shell monomers, as described in Sec. S5. Under conditions favorable for assembly, the droplet faces no thermodynamic barrier to growth; absent interactions with the shell, its radius R would increase at a constant average rate as cargo material arrives from the droplet's surroundings. Growth of the shell, on the other hand, is impeded by the energetic cost of wrapping an elastic sheet around a highly curved object. In early stages of this trajectory, shown in Fig. 1 (C), the cost of encapsulation is considerable, and the population of shell monomers remains small as a result.

As the droplet grows, and the curvature of its surface decreases, this elastic penalty diminishes and is eventually overwhelmed by attractions between shell and cargo. At a characteristic droplet size R^* , encapsulation becomes thermodynamically favorable. If the arrival rate of shell monomers is much higher than that of cargo (e.g., due to a higher concentration in solution), then a nearly complete shell will quickly develop, Fig. 1 (D), hampering the incorporation of additional cargo.

The nascent shell, while sufficient to block cargo arrival, is highly defective and far from closed. A slow healing process ensues, dominated by relaxation of grain boundaries between growth faces, Fig. 1 (E). This annealing process is, in part, achieved by relocating topological defects in the structure, a phenomenon that has been previously encountered in ground state calculations for closed elastic shells (29).

In the vast majority (87%) of the hundreds of assembly trajectories we have generated, healing leads ultimately to a completely closed structure with exactly 12 five-fold defects. Placement of these defects is often irregular and unlikely to yield minimum elastic energy, but further evolution of the structure is extraordinarily slow. Subsequent defect dynamics may produce more ideal shell structures as in Ref. (29), and transient shell opening may allow additional cargo growth; but these relaxation processes occur on much longer time scales. Our model microcompartments are equilibrated with respect to neither shell geometry nor droplet size, yet they are profoundly metastable, requiring extremely rare events to advance towards the true equilibrium state.

The scenario described above can be cast in a simpler light by considering as dynamical variables only the amounts of cargo and shell material in an idealized geometry. We focus on the radius R of a spherical droplet and the polar angle θ subtended by a contacting spherical cap of shell material, as depicted in Fig. 2 (A). In the spirit of classical nucleation theory, we estimate a free energy landscape in the space of R and θ through considerations of surface

tension and bulk thermodynamics. For our system these contributions include free energy of the condensed cargo phase, surface tension of a bare cargo droplet, free energy of a macroscopic elastic sheet, and line tension of a finite sheet, together with the energetics of shell bending and shell-cargo attraction. As shown in the Sec. S3, this free energy $F(R, \theta)$ can be written in the form

$$F(R, \theta) = a_c \left[\left(\frac{R}{R_c} \right)^2 - \left(\frac{R}{R_c} \right)^3 \right] + a_s \left[\left\{ \left(\frac{R^*}{R_s} \right)^2 - \left(\frac{R}{R_s} \right)^2 \right\} (1 - \cos \theta) + \frac{R}{R_s} \sin \theta \right], \quad (1)$$

where the energy scales a_c and a_s and the length scales R_c , R^* , and R_s (all of which can be related to parameters of the molecular model) transparently reflect the thermodynamic biases governing growth and encapsulation. The function $F(R, \theta)$ can be minimum only at $R = 0$ and $R = \infty$. As in the molecular model, finite microcompartments can appear and persist only as kinetically trapped nonequilibrium states.

Contours of this free energy surface, plotted in Fig. 2 (A), manifest the prohibitive cost of encapsulating small droplets. Only for radii $R > R^*$ is shell growth thermodynamically favorable. This characteristic length scale is determined by a straightforward balance among the shell's bending rigidity, the macroscopic driving force for flat shell growth, and the attraction between shell and cargo, as detailed in Sec. S3. Whether encapsulation occurs immediately once the droplet exceeds the critical size R^* depends on several kinetic factors. First, line tension of the sheet effects a barrier to encapsulation. As the droplet size increases, the height of this barrier declines, and encapsulation becomes facile only when it is sufficiently low. Second, the droplet may continue to grow while the shell develops. This latter possibility can be problematic: If the addition of shell material does not outpace that of cargo, then the angle θ decreases in time—the microcompartment grows but never advances towards closure, Figs. S5 and S6. Since the addition rate of cargo scales with the droplet's surface area, while the rate of adding shell material to an existing patch scales only with its perimeter, successful encapsula-

tion generally requires a substantial imbalance in addition rates, most easily achieved through a large excess of shell monomers in solution relative to cargo.

Dynamics on the free energy surface $F(R, \theta)$ illustrate this interplay of dynamical propensities. Stochastic trajectories, shown in Fig. 2 (A), were propagated with a kinetic Monte Carlo algorithm (Sec. S4). Here, the rates of adding cargo and shell material are biased not only by gradients in free energy, but also by geometric factors accounting for the number of available monomer addition sites and by an intrinsic imbalance in addition rates. The importance of the latter two kinetic effects is apparent through pathways that deviate strongly from simple gradient descent. In particular, θ increases rapidly at late times, despite equilibrium forces that encourage droplet growth at the expense of reduced shell coverage. When the shell is able to envelop the cargo with only modest changes in droplet size, the distribution of sizes can be quite narrow, as shown in Fig. 2 (B).

This phenomenological model explains the general course of our molecular assembly trajectories. But deviations from ideally spherical geometry, which are neglected in the reduced description, have notable mechanistic consequences. Fluctuations in cargo droplet shape that reduce local curvature can facilitate growth of a nearly flat shell patch over considerable areas even in the early stages of assembly. Enveloping the entire cargo globule nevertheless awaits sufficient cargo growth to reduce the average curvature below a threshold of roughly $1/R^*$. The necessary curvature that ultimately develops in the shell is also spatially heterogeneous. Protein sheets, which generally resist stretching more strongly than bending, tend to concentrate curvature at topological defects and along lines connecting them (30). As a kinetic consequence, bending is advanced primarily by discrete, localized events, in particular the formation of fivefold defects during shell growth. Indeed, the dynamics of encapsulation are noticeably punctuated by the appearance of topological defects, as seen in Movie S1.

Systems out of equilibrium often support rich spatial and temporal patterns, but in many

cases they are highly variable and challenging to harness or control. By contrast, the encapsulation process we have described is quite reliable. Fig. 3 (A) shows an unbiased selection of closed structures resulting from assembly trajectories of our molecular model. They are not perfectly icosahedral (Figs. S7 (A) and S7 (B)), echoing the discernibly nonideal geometries observed in electron micrographs of carboxysomes (25). Our assemblies are nonetheless roughly isotropic and distinctly faceted, as quantified by the distributions of sphericity and defect angles shown in Fig. 3 (B) and Fig. S7. Gently curved regions do sometimes appear, as they do in the laboratory. In our model this smoothness reflects the presence of paired defects (one fivefold and one sevenfold) that sometimes form in the process of shell closure, screening the elastic interactions that give rise to faceting (30).

In published (26) and concurrent work, Hagan et al. have computationally examined assembly dynamics of microcompartments stabilized by spontaneous curvature of the protein shell. Existing experimental data are not sufficient to judge whether carboxysome assembly is indeed guided by such a mechanically preferred curvature or, instead, yields shapes and sizes dictated by the explicitly nonequilibrium factors we have described. Quantitative characterization of the elastic properties of shell protein sheets in the absence of cargo would help decide this question. Similarly, a systematic measurement of microcompartment geometry as a function of protein concentrations would elucidate the role of dynamics in carboxysome assembly. Both of these perspectives suggest physically plausible strategies for nanoencapsulation with exciting prospects for synthetic realization. The nonequilibrium mechanism revealed by our model has a particularly minimal set of essential requirements: One needs only a monomer that assembles planar, elastic sheets and has an affinity for cargo that is prone to aggregation. Tuning concentrations of these constituents provides a direct route to generating monodisperse, nanoscale, controllably self-assembling structures.

References

1. B. B. Menon, Z. Dou, S. Heinhorst, J. M. Shively, G. C. Cannon, *PLOS ONE* **3**, e3570 (2008).
2. C. A. Kerfeld, S. Heinhorst, G. C. Cannon, *Annu. Rev. Microbiol.* **64**, 391 (2010).
3. F. Hinzpeter, U. Gerland, F. Tostevin, *Biophys. J* **112**, 767 (2017).
4. J. K. Polka, S. G. Hays, P. A. Silver, *Cold Spring Harb. Perspect. Biol.* **8**, a024018 (2016).
5. M. G. Mateu, *Arch. Biochem. Biophys.* **531**, 65 (2013).
6. J. M. A. Grime, *et al.*, *Nat. Commun.* **7**, 11568 (2016).
7. J. D. Perlmutter, M. F. Hagan, *Annu. Rev. Phys. Chem.* **66**, 217 (2015).
8. D. C. Rapaport, *Phys. Rev. Lett.* **101**, 186101 (2008).
9. R. Zandi, D. Reguera, R. F. Bruinsma, W. M. Gelbart, J. Rudnick, *Proc. Natl. Acad. Sci. U.S.A.* **101**, 15556 (2004).
10. A. Zlotnick, *J. Mol. Biol.* **241**, 59 (1994).
11. S. Whitelam, R. L. Jack, *Annu. Rev. Phys. Chem.* **66**, 143 (2015).
12. J. C. Cameron, S. C. Wilson, S. L. Bernstein, C. A. Kerfeld, *Cell* **155**, 1131 (2013).
13. S. Tanaka, *et al.*, *Science* **319**, 1083 (2008).
14. J. K. Lassila, S. L. Bernstein, J. N. Kinney, S. D. Axen, C. A. Kerfeld, *J. Mol. Biol.* **426**, 2217 (2014).
15. D. F. Savage, B. Afonso, A. H. Chen, P. A. Silver, *Science* **327**, 1258 (2010).

16. T. O. Yeates, Y. Tsai, S. Tanaka, M. R. Sawaya, C. A. Kerfeld, *Biochem. Soc. Trans.* **35**, 508 (2007).
17. T. A. Bobik, B. P. Lehman, T. O. Yeates, *Mol. Microbiol.* **98**, 193 (2015).
18. T. O. Yeates, C. S. Crowley, S. Tanaka, *Annu. Rev. Biophys.* **39**, 185 (2010).
19. F. Cai, M. Sutter, S. L. Bernstein, J. N. Kinney, C. A. Kerfeld, *ACS Synth. Biol.* **4**, 444 (2015).
20. R. Frey, S. Mantri, M. Rocca, D. Hilvert, *J. Am. Chem. Soc.* **138**, 10072 (2016).
21. T. W. Giessen, P. A. Silver, *Curr. Opin. Biotechnol.* **46**, 42 (2017).
22. C. Chen, *et al.*, *Nano Lett.* **6**, 611 (2006).
23. M. Sutter, B. Greber, C. Aussignargues, C. A. Kerfeld, *Science* **356**, 1293 (2017).
24. F. Cai, *et al.*, *PLOS ONE* **4**, e7521 (2009).
25. C. V. Iancu, *et al.*, *J. Mol. Biol.* **396**, 105 (2010).
26. J. D. Perlmutter, F. Mohajerani, M. F. Hagan, *eLife* **5**, 5342 (2016).
27. J. Wagner, R. Zandi, *Biophys. J* **109**, 956 (2015).
28. S. D. Hicks, C. L. Henley, *Phys. Rev. E* **74**, 031912 (2006).
29. C. M. Funkhouser, R. Sknepnek, M. Olvera de la Cruz, *Soft Matter* **9**, 60 (2013).
30. M. Bowick, A. Cacciuto, D. R. Nelson, A. Travesset, *Phys. Rev. Lett.* **89**, 185502 (2002).
31. J. Lidmar, L. Mirny, D. R. Nelson, *Phys. Rev. E* **68**, 051910 (2003).
32. H. S. Seung, D. R. Nelson, *Phys. Rev. A* **38**, 1005 (1988).

33. M. P. do Carmo, *Differential Geometry of Surfaces* (Springer Berlin Heidelberg, 1994).
34. J. N. Kinney, S. D. Axen, C. A. Kerfeld, *Photosynth. Res.* **109**, 21 (2011).
35. W. Humphrey, A. Dalke, K. Schulten, *J. Mol. Graphics* **14**, 33 (1996).
36. P. Steinhardt, D. Nelson, M. Ronchetti, *Phys. Rev. B* **28**, 784 (1983).

Acknowledgments

We thank Michael Hagan, Christoph Dellago, David Savage, Laura Armstrong, Avi Flamholz, and Luke Oltrogge for helpful conversations. GMR acknowledges support from National Science Foundation Graduate Research Fellowship and the James S. McDonnell Foundation. This work was supported by the US Department of Energy, Office of Basic Energy Sciences, through the Chemical Sciences Division (CSD) of the Lawrence Berkeley National Laboratory (LBNL), under Contract DE-AC02-05CH11231(PLG).

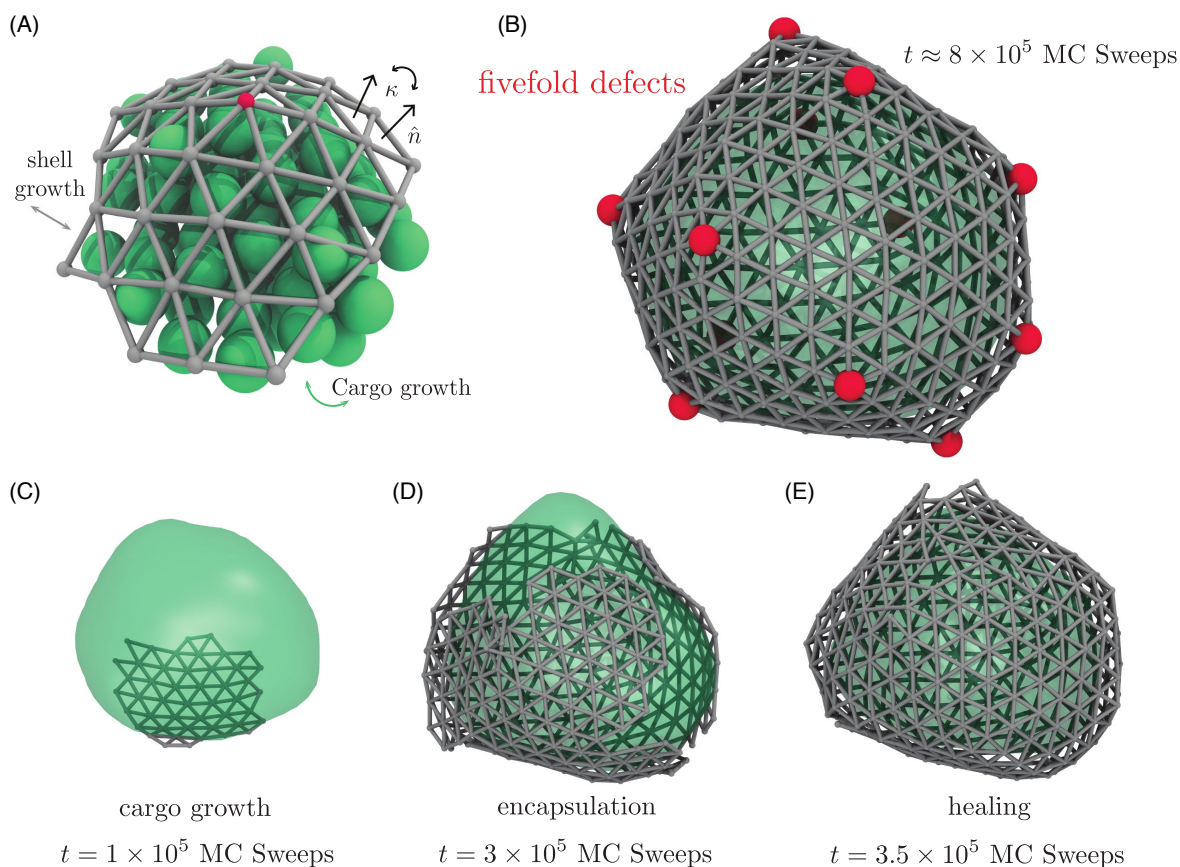


Figure 1: Model dynamics of microcompartment assembly. (A) Cargo monomers (green spheres) in our molecular model occupy sites of an FCC lattice, experiencing short-ranged attraction to their nearest neighbors and also to protein monomers comprising the shell. Each shell monomer corresponds to a triangle in a discretized sheet (gray) that resists bending and stretching according to an elastic Hamiltonian. Closure of the shell requires the presence of topological defects in the triangulated surface, vertices that are connected to only five neighbors. Red spheres here and in other figures highlight the locations of these defects. (B) A fully assembled microcompartment includes at least twelve of these defects. Here and in other figures, we show the boundary of the cargo droplet as a translucent green surface. (C) At early time t in the assembly process, high curvature of the cargo droplet limits shell growth to an area that is relatively flat while maintaining contact with the cargo. (D) Droplet growth reduces curvature until encapsulation becomes thermodynamically favorable and kinetically facile (Movie S1). (E) The nearly closed shell effectively halts cargo aggregation, but the approach to a simply connected envelope proceeds slowly as defects reposition and combine to heal grain boundaries.

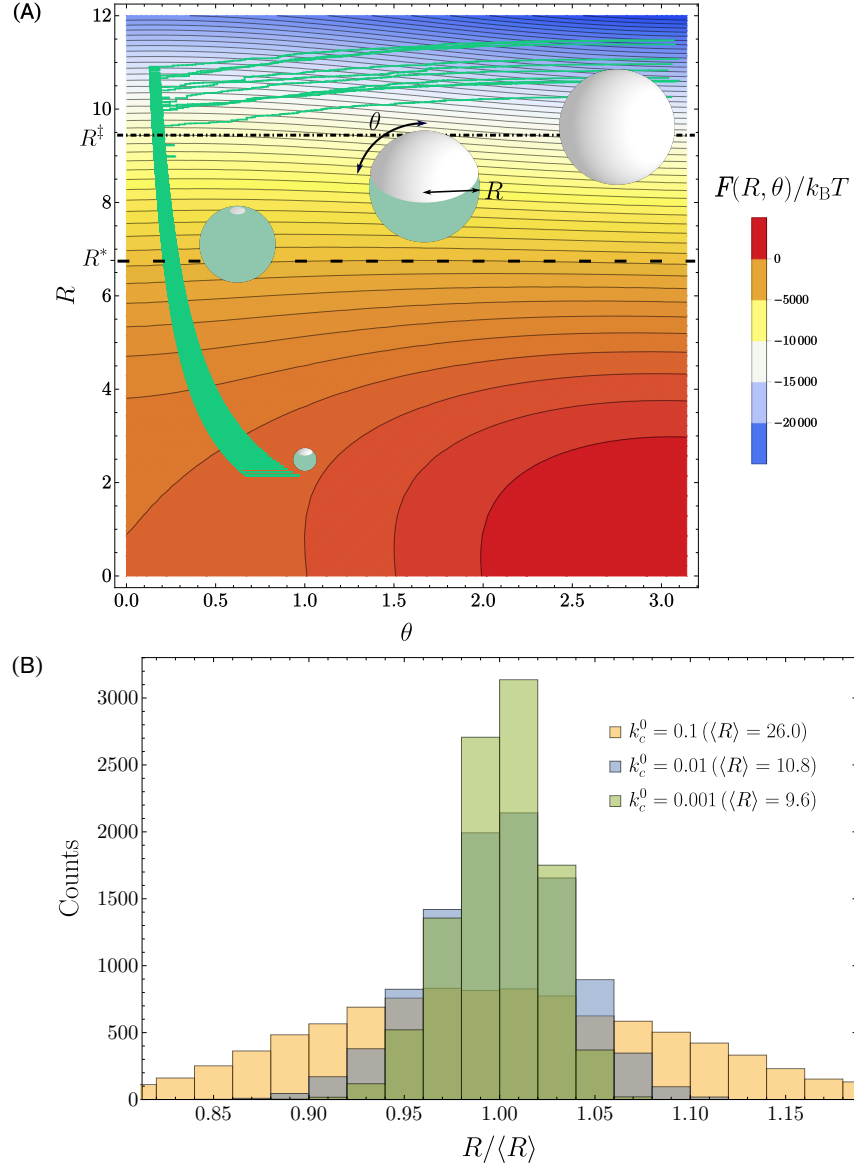


Figure 2: Reduced model for dynamics of cargo growth and encapsulation. (A) Our phenomenological model resolves only the radius R of a cargo droplet, and the polar angle θ of a spherical cap that coats it. Black contours indicate lines of constant free energy $F(R, \theta)$. Green lines show the course of ten kinetic Monte Carlo trajectories under conditions favorable for microcompartment assembly ($k_c^0/k_s^0 = 0.001$, all other parameters given in Sec. S4). Several structures along the assembly trajectory are shown near the corresponding values of R and θ . Encapsulation is thermodynamically favorable for $R > R^*$ (lower dashed line). The free energy barrier to encapsulation is smaller than the thermal energy $k_B T$ for $R > R^\ddagger$ (Eq. S63) (dot-dashed line). (B) Histograms of microcompartment radius when θ reaches π (at which point dynamics cease). Ten thousand independent trajectories were collected for $k_c^0/k_s^0 = 0.1$, 0.01, and 0.001.

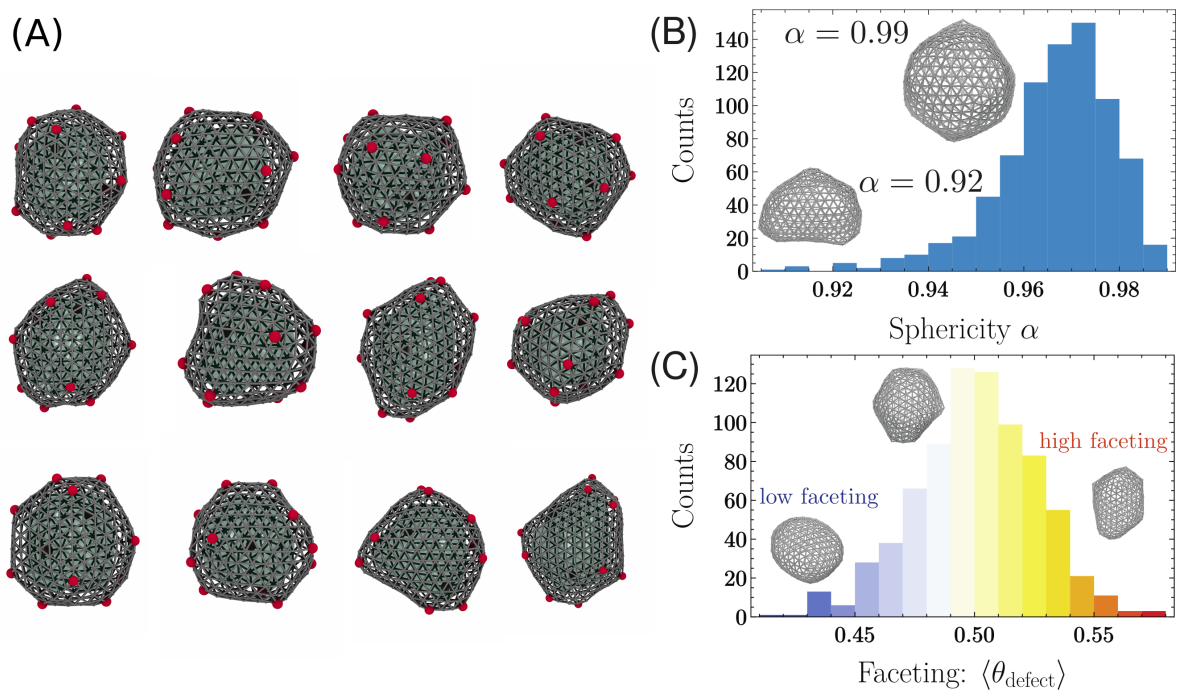


Figure 3: Structural variation among microcompartments generated by our molecular model. (A) Montage of twelve randomly selected structures. (B) Typical assemblies are not substantially elongated, as indicated by a histogram of the sphericity α (Sec. S7). (C) Faceting necessitates relatively sharp angles between shell monomers surrounding a fivefold defect (Sec. S7). A histogram of this angle $\langle \theta_{\text{defect}} \rangle$ (averaged over all defects in an assembled structure) underscores the typically strong faceting visible in (A).

Supplementary Materials

S1 Model energies

Our model of self-assembling microcompartments draws its principal features from standard statistical mechanics models of elastic sheets and aggregating solutes. In this section we detail our implementations, extensions, and combinations of these components.

S1.1 Shell

The continuum elasticity theory of a thin plate has been applied to biological protein assemblies, such as virus capsids, with surprising fidelity to the experimentally observed structures (31). A thin elastic membrane resists both stretching and out-of-plane fluctuations. Atomic resolution characterizations of carboxysome proteins have led researchers to suggest that pentamer defect generate curvature in an intrinsically flat, protein sheet (13). Following Ref. (32), we represent the total energy of a thin elastic membrane as a sum of these two contributions,

$$\mathcal{H} = \mathcal{H}_{\text{stretch}} + \mathcal{H}_{\text{bend}}, \quad (\text{S1})$$

We define a coordinate system that measures relative displacements,

$$u(x) = (u_1, u_2, z) \quad (\text{S2})$$

which maps $(x_0, y_0, 0)$ to $(x_0 + u_1, y_0 + u_2, z)$. This allows us to define a strain tensor,

$$u_{ij} = \frac{1}{2} (\partial_i u_j + \partial_j u_i + \partial_i z \partial_j z), \quad (\text{S3})$$

neglecting the terms quadratic in u_k . The stretching energy can be expressed in terms of Lamé coefficients μ_L and λ_L and the strain tensor u_{ij} ,

$$\mathcal{H}_{\text{stretch}} = \frac{1}{2} \int dS (2\mu_L u_{ij}^2 + \lambda_L u_{kk}^2). \quad (\text{S4})$$

The integral is taken over some parametrization of the surface of the membrane. Familiar material properties can be expressed in terms of the Lamé coefficients. For example, the Young’s modulus, which measures the tensile stress relative to the extensional strain of an in-plane deformation is

$$Y = \frac{4\mu_L (\mu_L + \lambda_L)}{2\mu_L + \lambda_L}. \quad (\text{S5})$$

The Poisson ratio, a material characteristic that relates the compression along the direction of an applied strain to the expansion along a transverse direction, is

$$\nu = \frac{\lambda_L}{2\mu_L + \lambda_L}. \quad (\text{S6})$$

These material properties determine, in part, the propensity of a thin elastic shell to “buckle”, developing visible, aspherical facets.

The bending contribution to the Hamiltonian enforces a quadratic cost to changes in the local curvature. Written in terms of the mean curvature H , the Gaussian curvature K , and the rigidities $\tilde{\kappa}$, $\tilde{\kappa}_G$, the bending energy is

$$\mathcal{H}_{\text{bend}} = \frac{1}{2} \int dS (\tilde{\kappa}H^2 + 2\tilde{\kappa}_G K). \quad (\text{S7})$$

The Gaussian curvature is a topological invariant, due to the Gauss-Bonnet theorem; it is ignored as an arbitrary constant in most analytical calculations (33). The continuum description of the membrane is particularly convenient for highly symmetrical objects, for which some calculations can be performed analytically. However, this formulation of the energy is not immediately applicable to the discrete growth of a nanoscale shell.

The elastic energy associated with the thin sheet can be discretized and expressed as a sum over the edges ij of a triangulated surface (32). The total Hamiltonian is,

$$\mathcal{H} = \frac{\epsilon}{2} \sum_{ij} (l_{ij} - l_0)^2 + \frac{\kappa}{2} \sum_{ij} 1 - \cos(\theta_{ij}), \quad (\text{S8})$$

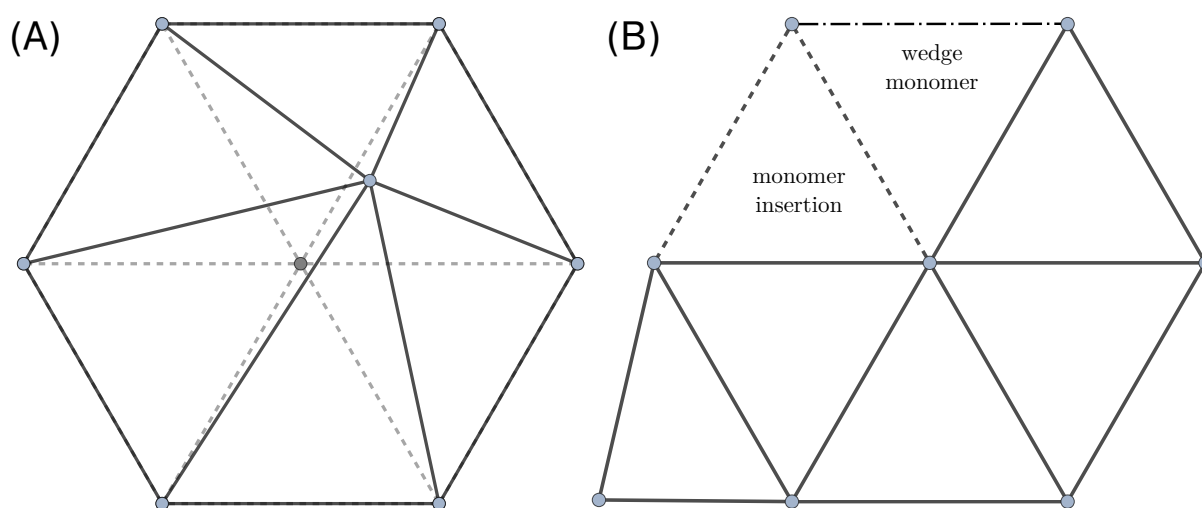


Figure S1: A schematic depiction of the vertex move proposal is shown in (A). Each vertex is randomly displaced and the energy difference between the initial and final states is computed. The move is then accepted or rejected so as to guarantee detailed balance. A schematic depiction of the monomer insertion move is shown in (B) A new monomer is added to the surface of the growing structure by randomly selecting a surface edge. The configuration of the inserted monomer is chosen randomly and the insertion is accepted in a detailed balance fashion.

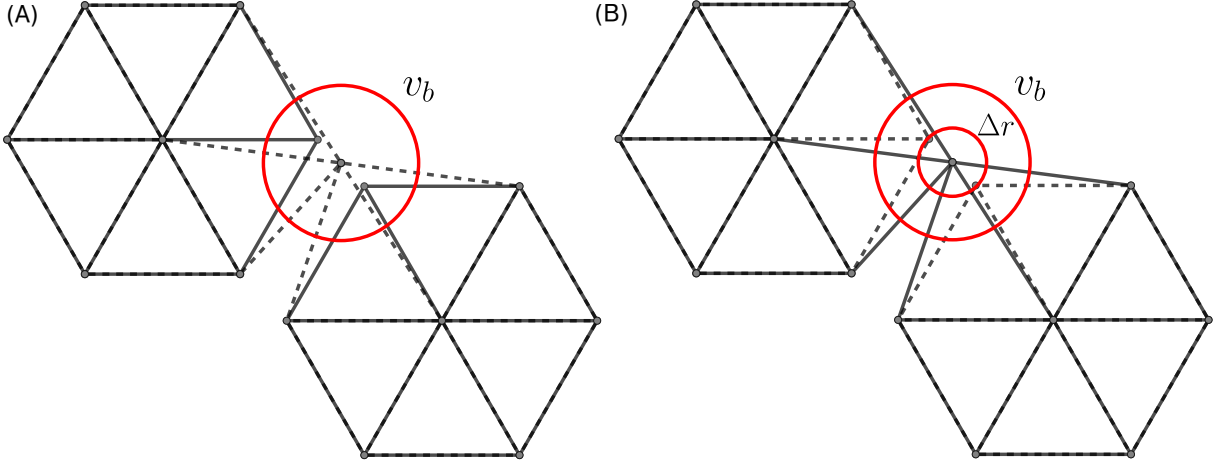


Figure S2: Schematics of vertex fusion and fission moves. In order to carry out fusion in a way that preserves detailed balance, we choose the fusion point randomly within some volume v_b , depicted in (A). The reverse operation, splitting vertices, requires choosing a pair of points separated by a randomly chosen distance Δr along a symmetric axis within the volume v_b , as shown in (B).

where ϵ is the renormalized stretching constant and $\kappa = \frac{2\sqrt{3}}{3}\tilde{\kappa}$ is the renormalized bending rigidity. The scalars relating the continuous and discrete Hamiltonians arise from a detailed analysis that involves taking the limit of infinitesimally small edge lengths so that the discretized Hamiltonian coincides exactly with continuum description of a thin elastic sheet. Such a calculation (32) exposes the precise relationship between ϵ and κ and the parameters of the continuum model. In particular, it has been shown,

$$Y = \frac{2\sqrt{3}}{3}\epsilon \quad \nu = \frac{1}{3} \quad (\text{S9})$$

$$\tilde{\kappa} = \frac{\sqrt{3}}{2}\kappa \quad \tilde{\kappa}_G = -\frac{4}{3}\kappa. \quad (\text{S10})$$

It is then possible to choose parameters in the discretized model that are consistent with the experimentally observed material properties of protein shells (31).

We associate each triangular face in our discrete lattice with a protein monomer. Because the deformations of the protein are expected to be small relative to the bending fluctuations

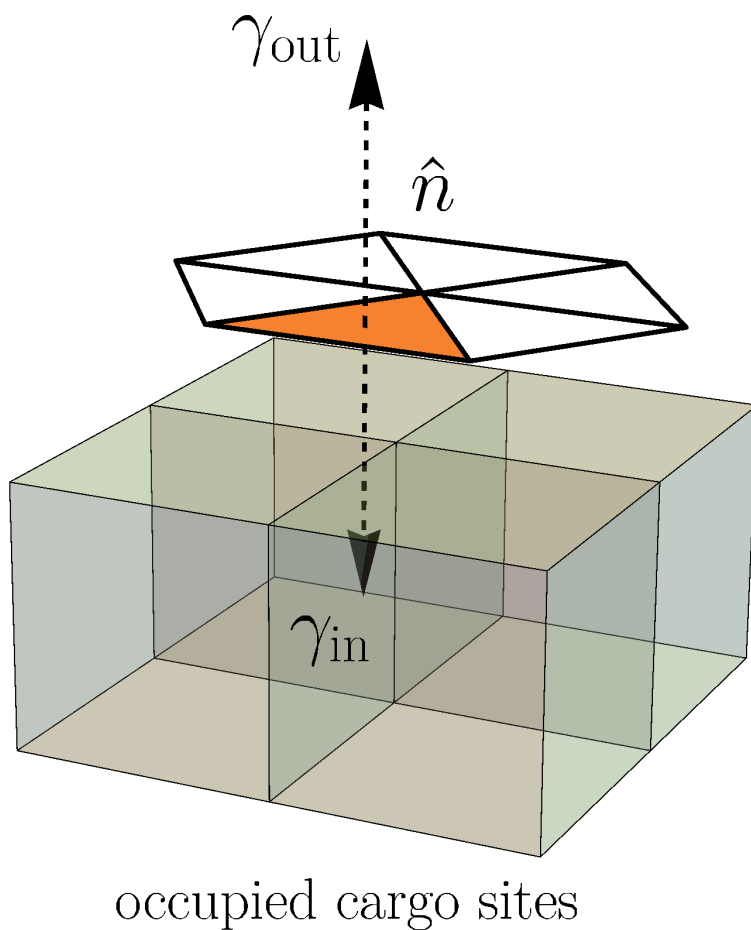


Figure S3: The cargo molecules, represented as a lattice gas, interact with the shell through an interaction that energetically favors the inward facing normal vectors with a factor $-\gamma_{in}$. The lattice site occupied by the outward facing normal vector of a monomer in the shell carries an energy γ_{out} , which serves to bias the shell fluctuations so that shell monomers are sterically occluded by the cargo.

between adjacent monomers, we work in a limit where $\epsilon l_0^2 \gg \kappa$. Previous calculations give further guidance on the elastic parameters: if we anticipate well-defined icosahedral structures, then we need to be in a regime where the ratio of the Young's modulus to the bending rigidity, scaled by the radius of the shell, is

$$Y R^2 / \kappa > 154, \quad (\text{S11})$$

the point at which a flat disk will be noticeably buckled around a defect. This ratio is called the Föppl-von Kármán number and is a measure of the relative cost of a stretching deformation to a bending deformation.

S1.2 Cargo

We represent aggregating cargo as an Ising lattice gas on an FCC lattice, allowing it fluctuate as a condensed droplet. Nearest neighbors are coupled through an interaction energy ϵ_C and chemical potential μ_C ,

$$\mathcal{H} = -\mu_C \sum_{i=1}^{N_c} \sigma_i - \epsilon_C \sum_{\langle ij \rangle} \sigma_i \sigma_j, \quad (\text{S12})$$

where $\sigma_i = \{0, 1\}$ for occupied and unoccupied lattice sites, respectively, and $\langle ij \rangle$ indicates that the sum is taken over nearest neighbors. The lattice spacing used throughout is l_0 , the average length of a shell monomer bond. In the carboxysome, the RuBisCO protein is larger than a shell monomer but choosing a finer lengthscale for the lattice spacing allows us to model in small lengthscale shape fluctuations in the cargo and its components.

S1.3 Cargo-shell interaction

We must further specify the nature of the cargo-shell interaction. In biological systems, any attraction between the proteins in the cargo and the proteinaceous shell will likely be short-ranged. Additionally, steric repulsions ensure that the shell proteins cannot overlap with the

cargo. To capture both features, we specify the cargo-shell interaction as follows

$$\mathcal{H}_{\text{int}}(\sigma_i, v_j) = \begin{cases} -\gamma_{\text{in}} & \text{if } -\hat{n}_j \in i \text{ and } \sigma_i = 1 \\ +\gamma_{\text{out}} & \text{if } \hat{n}_j \in i \text{ or } v_j \in i \text{ and } \sigma_i = 1 \\ 0 & \text{otherwise,} \end{cases} \quad (\text{S13})$$

where \hat{n}_i defines the outward facing normal vector to monomer j . The full interaction is the sum over all i and j of H_{int} . We have made the interaction directional because structural data has suggested a strong asymmetry or sidedness to carboxysome shell proteins (34). This interaction is depicted schematically in Fig. S3. There is an energetic benefit if the inward facing normal vector to the shell is within a cargo-occupied lattice site. Conversely, there is an energetic penalty if the outward facing normal vector lies within an occupied site.

S2 Monte Carlo dynamics of the model

The thermal relaxation of a shell with a fixed number of vertices and fixed connectivity, subject to the Hamiltonian discussed in the previous section, can be simulated with a straightforward Monte Carlo dynamics. In each move, a single vertex a of the lattice is chosen at random. As depicted in Fig. S1, a random perturbation in three-dimensional space is made to the selected vertex, giving a new coordinate a' . The energy difference, ΔE , which can be computed locally, is used in a standard Metropolis acceptance criterion,

$$\text{acc}(a \rightarrow a') = \min [1, \exp(-\beta\Delta E)]. \quad (\text{S14})$$

Following this procedure ensures that the configurations sampled in the Markov chain are consistent with a Boltzmann distribution.

The Monte Carlo move set for growth of the shell is significantly more involved. In order that the dynamics satisfy detailed balance, care must be taken throughout to ensure that every step is reversible and the generation probabilities are properly incorporated into the acceptance

criterion. Our goal is to draw samples from a grand canonical distribution,

$$p(X, N) = \Xi^{-1} \left(\frac{e^{\beta\mu}}{\lambda^9} \right)^N e^{-\beta E(X)}, \quad (\text{S15})$$

where Ξ denotes the grand canonical partition function, X gives the coordinates of the configuration, N is the number of monomers, and the length scale λ establishes a standard state for the monomer chemical potential μ . The factor λ^9 appears in the denominator because each monomer consists of three connected three-dimensional degrees of freedom. We define the “activity”,

$$z = \frac{e^{\beta\mu}}{\lambda^9}. \quad (\text{S16})$$

Developing a Monte Carlo move set that leaves this distribution invariant requires extreme care.

The simplest type of growth move that we implement is depicted in Fig. S1 (B). First, an edge at the surface of the growing sheet is selected at random; there are N_{surf} possible choices. A new monomer is proposed by initially generating an “ideal” insertion, i.e., a configuration that is aligned perfectly with the monomer to which it is attaching with edge lengths close to the equilibrium values. The newly inserted vertex is subsequently randomly selected within a volume v_b of the ideal center. This final step ensures that the procedure is statistically reversible.

In our model the vertices of bound monomers coincide exactly along the shared edge. The physical situation we have in mind is that separating such vertices by even a small distance r_a costs a large energy. For a favorable binding energy ϵ that is constant within the small volume $v_a = 4\pi r_a^3/3$, the affinity $K = v_a e^{-\beta\epsilon}$ completely characterizes the equilibrium statistics of binding. In setting $r_a = 0$, we implicitly take $\epsilon \rightarrow -\infty$ such that K remains nonzero and finite. We thus impose a well-defined binding equilibrium without resolving fluctuations of bound monomers on irrelevantly small scales. The constant K must be appropriately incorporated into the acceptance criterion for the growth move to ensure detailed balance.

We are working in a regime in which the Young’s modulus of the thin sheet is large. A

typical displacement of a vertex governed by the Hamiltonian \mathcal{H} of Eq. S8 is of order,

$$\delta \approx (\beta\epsilon)^{-1/2} \equiv \xi, \quad (\text{S17})$$

so we take ξ as a natural unit of length. We can then define a dimensionless affinity,

$$K^* = K\xi^{-3}. \quad (\text{S18})$$

The fusion moves discussed in detail later depend on K^* and v_{fuse}^* . We work in a limit where the probability of fission is small. Such near-irreversibility is often problematic for reliable self-assembly (11). For this system, however, configurations are rarely poised for fusion in highly distorted geometries. Furthermore, for a single connected sheet fusion can be effectively undone through a series of moves that do not involve fission. Accordingly, we choose another parameter,

$$f^* \equiv K^*/v_{\text{fuse}}^* \gg 1. \quad (\text{S19})$$

When f^* is large, the probability of accepting a proposed fusion move is large and, inversely, the probability of accepting a fission move is small. We note that fused edges can still be removed via monomer and wedge deletion moves.

The move that we have described generates a configuration X' from another configuration X which possesses one fewer monomer. In order to leave the distribution sampled by the Markov chain invariant, we must have

$$p(X \rightarrow X')p(X) = p(X' \rightarrow X)p(X') \quad (\text{S20})$$

The acceptance probability $\text{acc}(X \rightarrow X')$ for the insertion of a monomer must incorporate the generation probabilities $\text{gen}(X \rightarrow X')$ and $\text{gen}(X' \rightarrow X)$, corresponding to insertion and deletion, respectively, so that

$$p(X \rightarrow X') = \text{gen}(X \rightarrow X')\text{acc}(X \rightarrow X') \quad (\text{S21})$$

satisfies Eq. S20. We employ the Metropolis criterion for this purpose

$$\text{acc}(X \rightarrow X') = \min \left[1, \frac{\text{gen}(X' \rightarrow X)P(X')}{\text{gen}(X \rightarrow X')P(X)} \right]. \quad (\text{S22})$$

In some cases, it may be possible to insert a monomer by adding a single edge to the system, e.g., adding an edge between the top two vertices in Fig. S1. When a surface edge is selected at random, if a new monomer can be created by adding an edge of length $l < l_{\max}$ to another surface vertex, we propose the edge insertion move. The number of edges for which such a move is possible is N_{wedge} .

The generation probability for a monomer insertion is thus determined by the probability of selecting an eligible edge for monomer insertion that is not among the N_{wedge} edges

$$\text{gen}(X \rightarrow X') = \frac{1}{v_{\text{add}}(N_{\text{surf}}(X) - N_{\text{wedge}}(X))}. \quad (\text{S23})$$

This expression tabulates the probability of choosing a particular surface edge and point within the volume v_{add} , determined by the lengthscale l_{add} . The reverse move depends on selecting one of the two surface edges of a monomer with a single bound edge. The generation probability in the reverse direction is

$$\text{gen}(X' \rightarrow X) = \frac{1}{N_{\text{mono},1}(X')}. \quad (\text{S24})$$

where $N_{\text{mono},1}$ is the number of surface edges with a single bound edge in configuration X' , i.e., the set of monomers that could have been generated by a monomer insertion move.

The grand canonical probability of the configuration X' relative to the initial configuration is

$$\frac{p(X')}{p(X)} = zK^2 \exp(-\beta\Delta E), \quad (\text{S25})$$

where we have effectively integrated over binding fluctuations on the unresolved scale r_a . The factors of K resulting from this integration account for the binding energy and entropy of the vertices.

The energy difference ΔE can be computed locally and involves the elastic energy of the edges of the new monomer and the interaction with the cargo. The acceptance criterion for the insertion move is thus

$$\text{acc}(X \rightarrow X') = \min \left[1, zK^2 \frac{v_{\text{add}}(N_{\text{surf}}(X) - N_{\text{wedge}}(X))}{N_{\text{mono},1}(X')} e^{-\beta\Delta E} \right], \quad (\text{S26})$$

which acts as a guarantee of detailed balance.

The probability of proposing the monomer insertion moves with two bound edges depends only on N_{wedge}

$$\text{gen}(X \rightarrow X') = \frac{1}{N_{\text{wedge}}(X)} \quad (\text{S27})$$

The reverse move has a generation probability that is determined by the number of surface edges that have two bound edges, $N_{\text{mono},2}$, i.e., the set of monomer edges that could have been generated by the forward move. The acceptance criterion for insertion moves of this type is

$$\text{acc}(X \rightarrow X') = \min \left[1, zK^3 \frac{N_{\text{wedge}}(X)}{N_{\text{mono},2}(X')} e^{-\beta\Delta E} \right]. \quad (\text{S28})$$

Two nearby edges must also be able to join, to represent the binding of nearby edges. The likelihood of a vertex fusion event is determined by the favorable binding interaction described above. If there is a pair of unconnected surface vertices v and v' within a distance l_{fuse} , we attempt to join the vertices at their midpoint. In order for a fusion move to be proposed, the two vertices must either share a mutual neighbor or the involved surface edges must share a surface edge. Using the convention that K estimates the partition function of the bound vertices, we can specify an acceptance criterion that will lead to a detailed balance dynamics. The acceptance criterion depends on K and a volume v_b of a sphere with radius $l_{\text{fuse}}/2$,

$$\text{acc}(\text{fusion}) = \min \left[1, \frac{K}{v_b} e^{-\beta\Delta E} \right]. \quad (\text{S29})$$

The energy difference ΔE is due to bond stretching and bending resulting from the vertex fusion.

The simulations described here are in a regime where the reverse move, which we call vertex fission, is extremely unlikely. Nevertheless, we specify and implement it to ensure that we are sampling a well-defined distribution. The fission move is illustrated in Fig. S2. We select an eligible vertex v and choose a random point in the sphere of radius $l_{\text{fuse}}/2$, with a volume we call v_{fuse} . Not all surface vertices are eligible for fission. However, the set of fissionable vertices is precisely the set of fusible vertices, so there is no additional contribution to the acceptance criterion. This constraint only amounts to a detail in the implementation.

The random point we choose within the volume v_b designated as the location of one of the two new vertices. The other is uniquely determined, as well, because the midpoint of the vector connecting the new vertices is v . A randomly selected non-surface edge connected to v is duplicated and the neighbors of v become are split between the two new vertices. The acceptance criterion for the fission move can be constructed so that the dynamics obeys detailed balance. Its exact expression is

$$\text{acc}(\text{fission}) = \min \left[1, \frac{v_b}{K} e^{-\beta(\Delta E)} \right] \quad (\text{S30})$$

In practice, no fission moves occur in the course of a simulation owing to the relatively large values of K that, in the case of fission, are not counteracted by the activity z , though we have provided the implementation.

An additional set of Monte Carlo moves proposes changes to the lattice gas configuration ν representing the cargo droplet. In a growth move we choose one of the $N_{\text{surf}}(\nu)$ lattice sites adjacent to the boundary of the droplet, including the occupied boundary sites, and attempt to add or delete a cargo molecule. These moves are accepted with probabilities that respect a grand canonical distribution of cargo microstates,

$$p(\nu) \propto \exp [-\beta E(\nu) + \beta \mu_C N_C(\nu)]. \quad (\text{S31})$$

Specifically, detailed balance is imposed by accepting moves with probability,

$$\text{acc}(\nu \rightarrow \nu') = \min \left[1, \frac{N_{\text{surf}}}{N'_{\text{surf}}} e^{-\beta \Delta E + \beta \mu_C \Delta N_C} \right]. \quad (\text{S32})$$

Note that we impose artificial constraints of connectivity in these dynamics, i.e., there is only one connected droplet and only one connected sheet, neither of which may disappear entirely. This is done as a matter of convenience, with substantial computational savings. The constraint should not significantly affect assembly dynamics provided that nucleation of cargo and shell are both slow compared to their growth. The physical conditions we examine should fall in this regime.

Fivefold defects can spontaneously form as a consequence of fusion or monomer insertion moves. Sevenfold defects, on the other hand, we do not allow to form through monomer insertion or through typical fusion moves, because there is no evidence for sevenfold symmetric protein assemblies in the carboxysome literature. As the lone exception, a sevenfold defect may arise from fusion that causes two fivefold defects to share a neighbor. This arrangement can be viewed as accommodating a vacancy in the monomer sheet, rather than creating a heptameric arrangement of shell monomers. The large favorable energy for such a fusion event makes the distinction between vacancy and excess coordination thermodynamically unimportant.

S3 Phenomenological free energy

S3.1 Macroscopic equilibrium

In order to assess the equilibrium arrangements of cargo and shell species, we view their assembly as a chemical transformation, in which n shell capsomers S combine with m cargo subunits C to form a complex $A_{n,m}$, which might or might not be completely closed microcompartment. This process can be represented as a simple kinetic scheme



At thermodynamic equilibrium, stability criteria require that the chemical potentials μ associated with the constituent materials are balanced.

$$n\mu_s + m\mu_c = \mu_{n,m}. \quad (\text{S34})$$

Assuming these particles are present at very dilute concentration, the chemical potential of each species j can be written as a function of its density, the temperature T , and a density-independent standard state chemical potential $\mu^{(0)}$,

$$\mu_j(T) = \mu_j^{(0)}(T) + T \ln \frac{\rho_j}{\rho^{(0)}}. \quad (\text{S35})$$

Note that Boltzmann's constant has been absorbed into the unit of temperature, i.e., $k_B = 1$.

Combining the relationships above yields a law of mass action,

$$\rho_{n,m} = \rho^{(0)} \exp \left[-\beta \Delta\mu^{(0)} - nT \ln \frac{\rho_S}{\rho^{(0)}} - mT \ln \frac{\rho_C}{\rho^{(0)}} \right]. \quad (\text{S36})$$

The equilibrium constant relating densities of unassembled and assembled species is expressed here in terms of the reversible work required to assemble the components into a filled shell at standard state concentration,

$$\Delta\mu_{n,m}^{(0)} = \mu_{n,m}^{(0)} - n\mu_s^{(0)} - m\mu_c^{(0)}. \quad (\text{S37})$$

This simple relationship among particle densities allows us to investigate the equilibrium distribution of encapsulated structures. In particular, we ask at which value (n, m) the density $\rho_{n,m}$ is maximal.

Equivalently, we can find a minimum of the free energy

$$G(n, m) = \Delta\mu_{n,m}^{(0)} - nT \ln \frac{\rho_S}{\rho^{(0)}} - mT \ln \frac{\rho_C}{\rho^{(0)}}. \quad (\text{S38})$$

While an exact expression for G is not analytically tractable for our molecular model, we can judge from the energy scales involved what type of minima might exist. In particular, it is clear

that the shell-shell and cargo-shell interactions have an energy scale proportional to n while the cargo-cargo have an interaction energy proportional to m . Using these intuitive scaling arguments, we can postulate a simple expression for the free energy

$$G(n, m) = an + bm + E_{\text{el}}(n, m), \quad (\text{S39})$$

where the constants a and b are unknown functions of the densities, temperature, and binding free energies.

The elastic energy, in the case of an idealized spherical geometry, does not scale with the size of the shell; it is a constant $E_{\text{el}}(n, m) = 4\pi\kappa$. In the more general setting of nonspherical geometries, we can approximate the free energy as

$$G(n, m) = \nu m^{2/3} + bm + \text{const.} + E_{\text{el}}(\alpha), \quad (\text{S40})$$

where $\nu \equiv nm^{-2/3}$ is a parameter that quantifies the asphericity of the structure. Note that ν is not the same quantity used to characterize the sphericity in Sec. S7. A detailed analysis of the extrema of the free energy functional gives insight into the types of shapes that are thermodynamically preferred. The free energy has a minimum value $\nu_{\text{min}} = O(1)$ in which the structural is spherical. Because the elastic energy E_{el} is an increasing function of ν , the minimum of the free energy will have $\nu = \nu_{\text{min}}$ for a fixed m , so long as $a > 0$. As a result, global minima of the free energy can only occur at $m = 0$ or $m = \infty$, depending on the sign of b . Mathematically, negative values of a could produce minima, but such a negative surface tension would result in highly distended shapes, which are not physically relevant for our model. A similar scaling argument can be made for idealized icosahedral structures. This implies that the metastable microcompartment structures seen in biological systems must represent a departure from equilibrium statistics.

S3.2 Thermodynamic potential for compartment size and shell coverage

A more detailed phenomenological free energy functional can be constructed by assuming that cargo-shell assemblies adopt the simple geometry suggested by the analysis above. Specifically, cargo molecules are assumed to form a compact spherical globule, and the shell proteins are assumed to coat the globule as a spherical cap. At the level resolved here, icosahedral structures would be governed by a very similar potential.

It is convenient to write this functional in terms of the radius of the spherical cargo droplet, R , and the angle subtended by the spherical cap θ . We let f_c denote the free energy per unit cargo and γ_c the surface tension associated with the condensed cargo droplet. Similarly, we define f_s and γ_s as the free energy per unit shell and the line tension around the growth edge of the shell. The variables ρ and σ denote the density and surface density of the cargo and the shell proteins, respectively. The interaction energy is $-\epsilon$ per monomer. The elastic energy is determined by a bending rigidity κ . Finally, the activity of the cargo monomers is z_c and the activity of the shell monomers is z_s . Putting together all the terms, we have

$$F(R, \theta) = \frac{4}{3}\pi R^3 \rho (f_c - T \ln z_c) + 2\pi R^2 (1 - \cos \theta) \sigma (f_s - T \ln z_s - \epsilon) + 4\pi R^2 \gamma_c + 2\pi R \sin \theta \gamma_s + 2\pi \kappa (1 - \cos \theta). \quad (\text{S41})$$

The fully assembled microcompartment is stable when $\Delta F_{\text{close}}(R) \equiv F(R, \pi) - F(R, 0)$ becomes negative. If the rate of cargo growth is much slower than the rate of shell growth, the expected size of the assembly is

$$R^* = \sqrt{\kappa / |\sigma (f_s - T \ln z_s - \epsilon)|} \quad (\text{S42})$$

Both the shell and the cargo may need to overcome nucleation barriers before they begin growing spontaneously. In practice, this means that the expected size of the completely assembled structure will depend on the height and location of these barriers. The free energy F can

be written in a form that highlights the connection to classical nucleation theory as

$$F(R, \theta) = a_c \left[\left(\frac{R}{R_c} \right)^2 - \left(\frac{R}{R_c} \right)^3 \right] + a_s \left[\left\{ \left(\frac{R^*}{R_s} \right)^2 - \left(\frac{R}{R_s} \right)^2 \right\} (1 - \cos \theta) + \frac{R}{R_s} \sin \theta \right], \quad (\text{S43})$$

with

$$a_s = \frac{2\pi\gamma_s^2}{\sigma(T \ln z_s + \epsilon - f_s)} \quad (\text{S44})$$

$$R_s = \frac{\gamma_s}{\sigma(T \ln z_s + \epsilon - f_s)} \quad (\text{S45})$$

$$a_c = \frac{36\pi\gamma_c^3}{\rho^2(f_c - T \ln z_c)^2} \quad (\text{S46})$$

$$R_c = \frac{3\gamma_c}{\rho(T \ln z_c - f_c)} \quad (\text{S47})$$

$$R^* = \sqrt{2\pi\kappa} R_s. \quad (\text{S48})$$

This expression highlights the characteristic sizes of the critical nuclei and their interconnected dependence on the microscopic parameters. In particular, it should be noted that for the parameters that we are exploring the cargo has essentially no barrier to nucleation, whereas the shell has a significant one at small radius. However, as the radius increases, the shell can grow with greater facility and encapsulation becomes kinetically accessible.

The average size of an encapsulated structure depends strongly on the bending rigidity κ . Fig. S4 emphasizes that, even for large average radii, the distribution of sizes can be made tight by decreasing the rate of cargo addition. In principle, the average size of the structure could be tuned by controlling material properties of the constituent monomers, though this is likely a difficult engineering problem in practice.

S4 Kinetic Monte Carlo

The phenomenological free energy Eq. S41 does not prescribe a particular dynamics. In order to simulate the dynamics of encapsulation and cargo growth on this free energy surface, we first

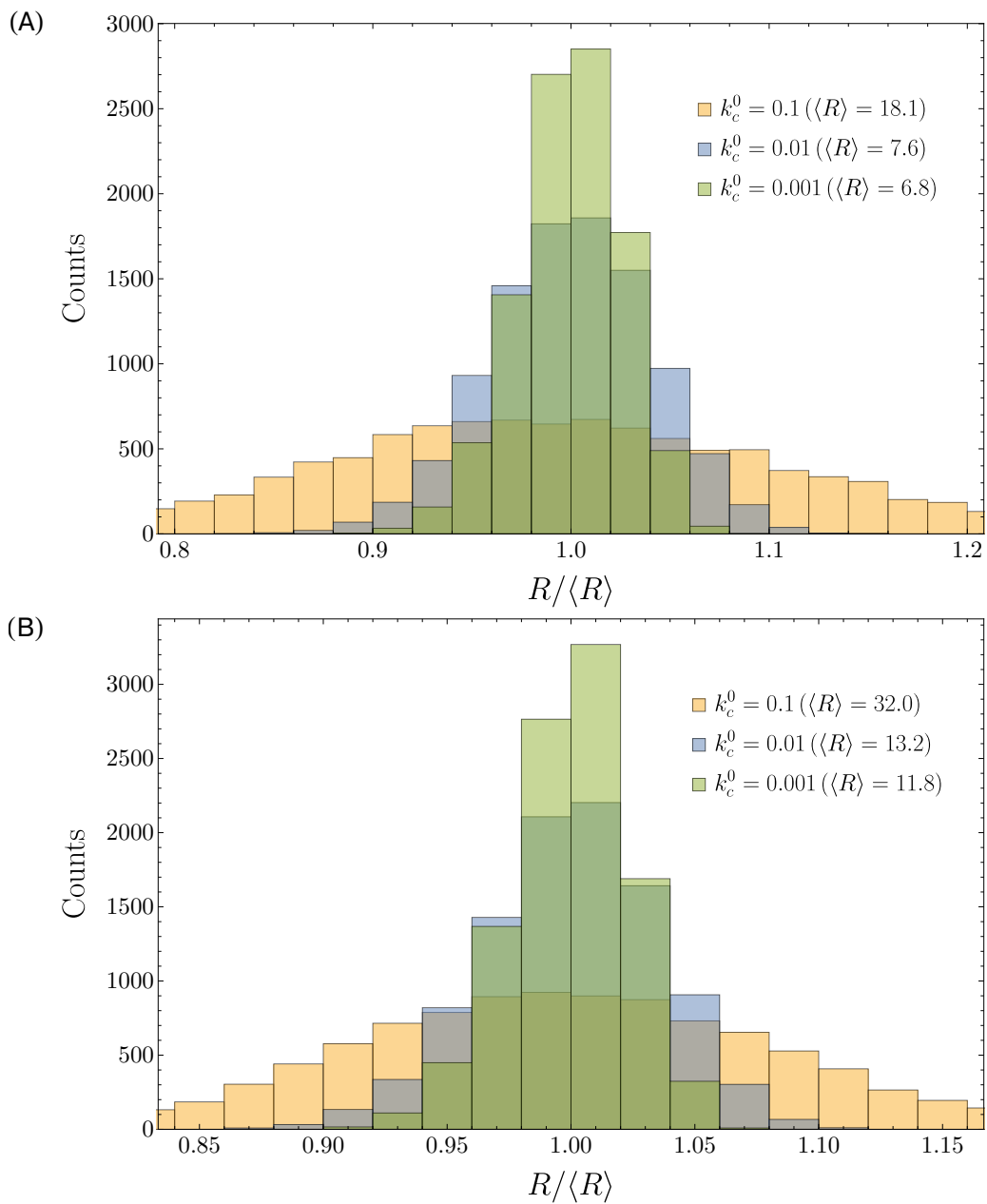


Figure S4: Histograms of the radii of the encapsulated structures computed from kinetic Monte Carlo simulations. (A) $\kappa = 100$. (B) $\kappa = 300$. Throughout $k_s^0 = 1$. Data was collected from 10^4 independent KMC simulations.

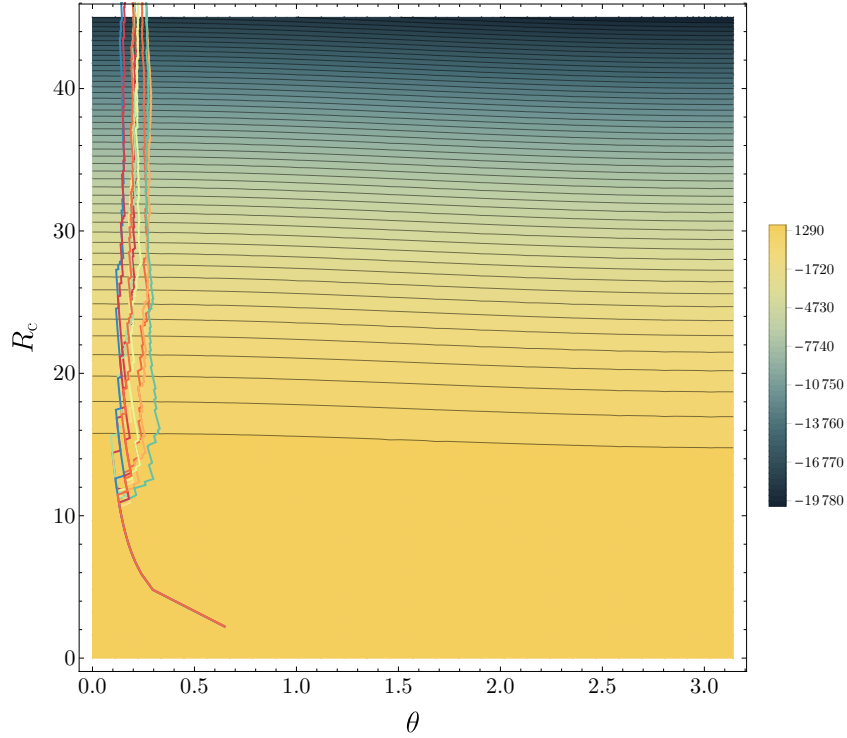


Figure S5: Trajectories illustrating runaway growth. The cargo arrival rate is $k_c^0 = 1$ and the shell arrival rate is $k_s^0 = 1$. The trajectories do not encapsulate after 10^6 steps of KMC dynamics.

associate with the shell and cargo rates k_s^0 and k_c^0 at which monomers arrive at a given site where they may add (and assume that all such arrivals lead to successful monomer incorporation). These rates should be understood to depend, in part, on the chemical potentials μ_s and μ_c . In addition to these arrival rates of material addition, we must also account for geometric factors proportional to the number of growth edges available for shell addition and the surface area available for additional cargo growth. In terms of the variables R and θ , the geometrically modified rates are,

$$k_s(R, \theta) = k_s^0 R \sin \theta \quad (\text{S49})$$

$$k_s(N_s, N_c) = k_s^0 \sqrt{2N_s - N_s^2 N_c^{-2/3}} \equiv k_s^+(N_s, N_c) \quad (\text{S50})$$

and

$$k_c(R, \theta) = k_c^0 4\pi R^2 (1 - \cos \theta) \quad (\text{S51})$$

$$k_c(N_s, N_c) = k_c^0 (4\pi N_c^{-2/3} - 2\pi N_s) \equiv k_c^+(N_s, N_c), \quad (\text{S52})$$

which are proportional to the accessible surface area of the cargo and the surface edge length of the shell.

The ratio of addition and removal rates is completely specified by the constraint of detailed balance. Defining the shell monomer and cargo monomer free energy differences

$$\Delta G_s = G(N_s, N_c) - G(N_s - 1, N_c), \quad (\text{S53})$$

$$\Delta G_c = G(N_s, N_c) - G(N_s, N_c - 1), \quad (\text{S54})$$

$$(\text{S55})$$

we require that the rates of monomer removal satisfy

$$k_s^-(N_s, N_c) = k_s^+(N_s - 1, N_c) e^{\beta \Delta G_s}, \quad (\text{S56})$$

and

$$k_c^-(N_s, N_c) = k_c^+(N_s, N_c - 1) e^{\beta \Delta G_c}. \quad (\text{S57})$$

Simulations were initialized with $N_s = 1$ and $N_c = 10$. We employed the constraint that $N_s \geq 1$, i.e., the shell material was prohibited from disappearing entirely. Simulations were halted when $N_s \geq 2N_c^{2/3}$, when the shell entirely covered the spherical cargo.

S5 Simulations of the molecular model

All simulations were performed using an implementation of the algorithm described in Section S2 which is available on github (link to be inserted upon publication). The parameters used for all simulations are described in Tables S2 and S3.

Table S1: Simulation parameters for the FCC lattice gas cargo.

ϵ_C	100.
μ_C	-500.
γ_{in}	1.0
γ_{out}	600.
T	80.
k_c^0	0.000075

Table S2: Simulation parameters for the elastic shell model.

ϵ	800.
κ	30.
l_0	1.
l_{max}	1.5
l_{min}	0.5
l_{fuse}	0.25
l_{add}	0.25
$\ln K$	3
$\ln z$	-12
k_s^0	0.0075

All simulations were initialized with a hexamer of shell material which we did not allow to be removed. This ensures that nucleation of the shell can occur. Cargo is initiated by populating all lattice sites within three lattice spacings of the origin (corresponding to a total number 429 of cargo monomers).

Each Monte Carlo sweep of the simulation involves N_v attempted elastic relaxation moves. The growth moves for the shell are proposed in proportion to the number of surface shell monomers, i.e., the number of available growth edges. We scale this number by a kinetic parameter k_s^0 , an analogue of the base rate of addition in the kinetic Monte Carlo simulations. It should be noted that the rate of addition could alternatively be tuned by changing the activity z . Similarly, the growth moves for the cargo are proposed in proportion to N_{surf} scaled by the parameter k_c^0 .

The simulation completes when there are no remaining surface edges on the shell structure. At this point, growth moves are no longer proposed and the structure is equilibrated for 10^5 MC sweeps before exiting. An animation of a trajectory of the microscopic model is shown in Movie S1.

Simulations were visualized using the VMD software package (35). In order to clearly show the shell structure, only occupied lattice sites that are above a distance cutoff of $1.5l_0$ are shown in our visualizations. The cargo is depicted either as density isosurfaces or spheres centered at the lattice sites. In the Movie S1, the shell is depicted as dynamic bonds with a distance cutoff of $1.5l_0$, which leads to unconnected vertices appearing bonded in some frames.

S6 Dynamical flows

In very simple models, the routes of typical trajectories can be inferred directly from the underlying free energy surface. Kinetic inference is not so straightforward for our models. Dynamical flows are complicated by geometric factors described in the previous section, e.g., the fact that

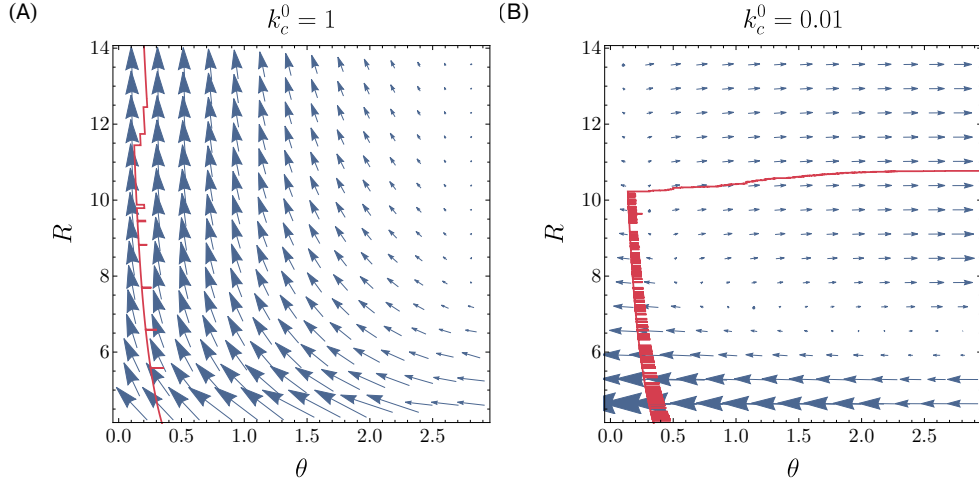


Figure S6: Flow vectors $\omega = (\dot{\theta}, \dot{R})$ are plotted with representative trajectories. The size of the vector is proportional to its magnitude. In both cases, $\kappa = 200$ and the shell arrival rate $k_s^0 = 1$. (A) A representative trajectory with $k_c^0 = 1$ is shown in red below the vector field. (B) A representative trajectory with $k_c^0 = 0.01$ is shown in red below the vector field.

cargo addition rates are proportional to the number of available surface sites, which changes during the course of assembly. The free energy $F(R, \theta)$ in this case constrains ratios of rates for each forward and reverse move, but does not give a good sense for the directions along which the system typically evolves.

In this section we develop a means to visualize dynamical tendencies for cargo droplet growth and shell envelopment in our phenomenological model. Let $\omega(\theta, R)$ be a vector field with components $\omega_R = \dot{R}$ and $\omega_\theta = \dot{\theta}$ along R and θ that reflect the typical rate of change along these coordinates at each point in the θ, R -plane. First, we differentiate the relationships

$$R(N_c) = \left(\frac{3}{4\pi} \rho^{-1} N_c \right)^{1/3} \quad (\text{S58})$$

$$\theta(N_s, N_c) = \cos^{-1} \left(1 - \frac{N_s}{2\pi\sigma R(N_c)} \right), \quad (\text{S59})$$

to express the time derivatives \dot{R} and $\dot{\theta}$ in terms of R , θ , \dot{N}_s and \dot{N}_c , where dots represent differentiation with respect to time. We then estimate average rates of change in N_s and N_c

through the effective drift in these populations,

$$\dot{N}_s = -k_s^+(N_s, N_c) \frac{\partial G}{\partial N_s} \quad (\text{S60})$$

$$\dot{N}_c = -k_c^+(N_s, N_c) \frac{\partial G}{\partial N_c}, \quad (\text{S61})$$

which can in turn be written in terms of R and θ . Plotting ω as a function of R and θ yields a dynamical flow field that reveals the direction in which trajectories typically evolve from each point (θ, R) .

The dynamical flow fields shown in Fig. S6 highlight the importance of monomer arrival rates, particularly for the likelihood of shell closure. Panels (A) and (B) correspond to systems with the same free energy $F(R, \theta)$, but with different relative arrival rates, k_c^0 , for cargo.

For very fast cargo arrival, the nucleation of sufficient shell material to encapsulate the rapidly expanding surface of the cargo is kinetically impeded. The field shown in Fig. S6 (A) corresponds to this case of “runaway” growth (see also, Fig. S5), with ω pointing primarily in the direction of increasing R throughout much of (θ, R) space. In a typical trajectory, the radius of the cargo increases rapidly and the angle θ cannot grow to fully encapsulate the surface.

By contrast, when the shell arrival rate greatly exceeds that of cargo, the field points more strongly along increasing θ , promoting shell closure. As soon as the barrier to nucleating a shell disappears, the average dynamical flow leads trajectories rapidly and unequivocally towards encapsulation, as shown in Fig. S6 (B). This representation of dynamical biases does not capture the possibility of barrier crossing, i.e., the spontaneous nucleation of a substantial shell even when it requires activation. In these systems, however, this nucleation barrier becomes comparable to $k_B T$, and therefore easily navigated, not far from the point where shell growth becomes thermodynamically downhill.

The location of the barrier $\theta^\ddagger(R)$, for a given droplet radius R , can be determined by finding

the maximum of $\frac{\partial F(R,\theta)}{\partial \theta}$ in the range $[0, \pi]$. Using the resulting expression,

$$\theta^\ddagger(R) = \tan^{-1} \left(\frac{\frac{R}{R_s}}{\left(\frac{R}{R_s}\right)^2 - \left(\frac{R^*}{R_s}\right)^2} \right), \quad (\text{S62})$$

we can estimate the radius at which the barrier to shell growth becomes comparable to the thermal energy. We judge the height of the barrier,

$$\Delta F^\ddagger(R) = F(R, \theta^\ddagger) - F(R, \theta_0), \quad (\text{S63})$$

with reference to a typical value $\theta_0 = 0.2$ of the spherical cap angle prior to nucleation of a steadily growing shell. This activation free energy becomes comparable to thermal energy at a radius R^\ddagger for which

$$\Delta F^\ddagger(R^\ddagger) = k_B T. \quad (\text{S64})$$

The critical radius R^\ddagger compares favorably with the point at which shell nucleation occurs in kinetic Monte Carlo simulations, as shown in Fig. 2 (A).

S7 Quantifying size and shape distributions

We quantified the size of assembled microcompartments according to their “effective” radii. We defined the effective radius as

$$R_{\text{eff}} = \left(\frac{3N_c}{4\pi} \right)^{1/3}, \quad (\text{S65})$$

which assumes an idealized spherical droplet. While this measure of the radius is only approximate, it readily provides insight into the degree of size heterogeneity.

In order to quantify the extent of shape fluctuations, we computed both a measure of sphericity and a measure of the ideality of the icosahedral shape. We measure the sphericity by quantifying deviations from the mean radius. Let \mathbf{r}_0 denote the center of mass of the vertices. We

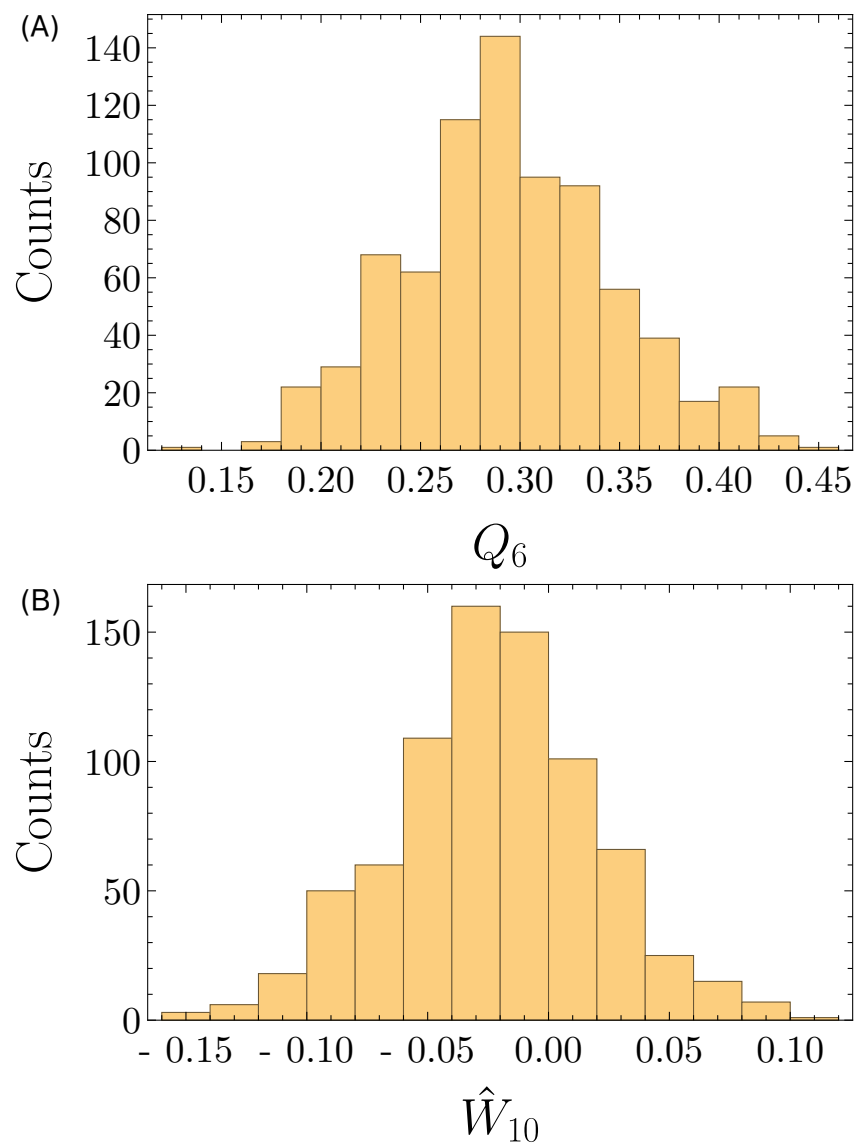


Figure S7: Histograms of Q_6 and \hat{W}_{10} from final structures of the simulations of the microscopic model.

denote by d_i magnitude of the vector \mathbf{r}_i which connects \mathbf{r}_0 to a vertex indexed by i . Then the sphericity is calculated as

$$\alpha(\mathcal{V}) = 1 - \sum_{i \in \mathcal{V}} (\langle d_i^2 \rangle - \langle d_i \rangle^2) / \langle d_i \rangle. \quad (\text{S66})$$

The number α is 1 on a perfect sphere. As the variance of the distance to shell grows, the value of the order parameter decreases. This parameter is not strongly influenced by the presence of sharp edges and vertices, but instead characterizes the extent to which a structure is isotropic rather than distended or elongated.

Bond orientational order parameters (cf. Ref. (36)) provide a very sensitive measure of icosahedral symmetry. We computed the distribution of two such parameters that distinguish icosahedral orientational order from face-centered cubic, body-centered cubic, hexagonal close packed, and simple cubic packings. Following Steinhardt et al., we define

$$Q_6(\{r_1, \dots, r_{N_{\text{defect}}}\}) = \frac{1}{N_{\text{defect}}} \sum_{i=1}^{N_{\text{defect}}} \sum_{l=-m}^m Y_{6m}(r_i) \quad (\text{S67})$$

and

$$\hat{W}_{10} = \sum_{m_1, m_2, m_3 = -l, \dots, l} \begin{pmatrix} l & l & l \\ m_1 & m_2 & m_3 \end{pmatrix} \frac{Q_{l, m_1} Q_{l, m_2} Q_{l, m_3}}{\left(\sum_{m=-l}^l Q_{lm} \right)^{3/2}}, \quad (\text{S68})$$

where the coefficient is the Wigner 3- j symbol. For an ideal icosahedral structure

$$Q_6 \approx 0.66 \quad \hat{W}_{10} \approx -0.094 \quad (\text{S69})$$

Previous studies have classified icosahedrality using a minimum of 0.6 for Q_6 or a maximum of -0.1 for \hat{W}_{10} . By these metrics, our typical structures deviate strongly from perfect icosahedra. The distribution of \hat{W}_{10} suggests that some structures reasonably approximate ideal icosahedra, but those structures are rare, in the tail of the distribution of Fig. S7. In contrast, the Q_6 order parameter does not register icosahedrality in our structures, as seen in Fig. S7.

Though the structures are clearly not ideal icosahedra, they have the distinct faceted appearance of the structures typically seen in tomograms of carboxysomes and other bacterial microcompartments. To quantify the extent to which the structure is faceted, it is useful to look at the extent of bending in the proximity of fivefold defects. We use the average bending angle of the five bonds around a defect as a faceting measure. Let \mathcal{V}_d denote the set fivefold defect vertices in a structure, of which there are N_d . We also define $\mathcal{B}(v_i)$ to be the set of bonds connected to vertex v_i which has elements ij . Then, the faceting parameter is

$$\langle \theta_{\text{defect}} \rangle = \frac{1}{5N_d} \sum_{v_i \in \mathcal{V}_d} \sum_{ij \in \mathcal{B}(v_i)} |\theta_{ij}|. \quad (\text{S70})$$